

2401 **Chapter 8**
2402 **Weak Focusing Synchrotron**

2403 **Abstract** This Chapter is a brief introduction to the weak focusing synchrotron,
2404 and to the theoretical material needed for the simulation exercises. It relies on basic
2405 charged particle optics and acceleration concepts introduced in the previous Chap-
2406 ters, and further addresses

- 2407 - fixed closed orbit,
- 2408 - periodic structures,
- 2409 - periodic stability,
- 2410 - optical functions,
- 2411 - synchrotron motion,
- 2412 - depolarizing resonances.

2413 The simulation of weak synchrotrons only require a very limited number of opti-
2414 cal elements; actually two are enough: DIPOLE or BEND to simulate combined
2415 function dipoles, and DRIFT. Particle monitoring requires keywords introduced in
2416 the previous Chapters, including FAISCEAU, FAISTORE, possibly PICKUPS. Spin
2417 motion computation and monitoring resort to SPNTRK, SPNPRT, FAISTORE,

2418 **Notations used in the Text**

$B; \mathbf{B}; B_x, B_y, B_s$	field value; field vector; components
$B\rho = p/q; B\rho_0$	particle rigidity; reference rigidity
C	closed orbit length, $C = 2\pi R$
E	particle energy
EFB	Effective Field Boundary
f_{rf}	RF frequency
h	RF harmonic number
$m; m_0; M$	mass; rest mass; in units of MeV/c^2
$n = \frac{\rho}{B} \frac{dB}{d\rho}$	focusing index, a local quantity
$\mathbf{p}; p_0$	particle momentum vector; reference momentum
P_i, P_f	initial, final asymptotic polarization at traversal of a spin resonance
q	particle charge
r	orbital radius
R	average radius, $R = C/2\pi$
2419 s	path variable
v	particle velocity
$V(t); \hat{V}$	oscillating voltage; its peak value
x, x', y, y'	radial and axial coordinates in Serret-Frénet frame
$\beta = v/c; \beta_0; \beta_s$	normalized particle velocity; reference; synchronous
$\gamma = E/m_0$	Lorentz relativistic factor
$\Delta p, \delta p$	momentum offset
ε_u	Courant-Snyder invariant (u: x, r, y, l, Y, Z, s, etc.)
ϵ_R	strength of a depolarizing resonance
$\phi; \phi_s$	particle phase at voltage gap; synchronous phase
ϕ_z	betatron phase advance, z stands for x or y
φ	spin angle to the vertical axis
$\langle A \rangle; \langle A \rangle _u$	average of A; over variable u

2420 **Introduction**

2421 The synchrotron came on the scene as an application of 1945's phase focusing [1, 2]
 2422 concept. The latter states that off-crest acceleration with proper phase of the voltage
 2423 oscillation at arrival of a particle at the accelerating gap results in stable longitudinal
 2424 motion, "longitudinal focusing", around a stable, fixed, "synchronous phase". The
 2425 reference orbit in a synchrotron on the other hand, is maintained at constant radius
 2426 by ramping the guide field in synchronism with the acceleration, a concept already
 2427 familiar at the time with the betatron [3].

2428 Phase focusing was demonstrated experimentally in 1946 using a cyclotron
 2429 dipole [4]. Demonstration of phase stability at constant orbital radius followed in

2430 1946, using an existing betatron ring [5]. Due to the cycling of the acceleration, a
 2431 synchrotron accelerates particle bunches, comprised of particles that have proper
 2432 relationship, in both frequency and phase, with the oscillating voltage at the acceler-
 2433 ating gap, or gaps around the ring. The concept allowed greatest energy reach, it led
 2434 to the construction of a series of proton rings with increasing energy: 1 GeV at Birm-
 2435 ingham (1953), 3.3 GeV at the Cosmotron (BNL, 1953), 6.2 GeV at the Bevatron
 2436 (1954), 10 GeV at the Synchro-Phasotron (Dubna, 1957), and a few additional ones
 2437 beyond 1952~1953, into the era of the technology which would essentially dethrone
 2438 it: the strong focusing synchrotron. The general layout of these first synchrotrons
 2439 included straight sections (often 4, Fig. 8.1), which allowed insertion of injection
 2440 (Fig. 8.2) and extraction systems, accelerating cavities, orbit correction and beam
 2441 monitoring equipment.

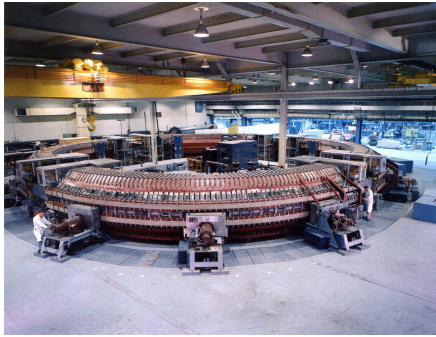


Fig. 8.1 The Cosmotron at BNL, reached its full design energy of 3.3 GeV in 1953. It was used until 1968

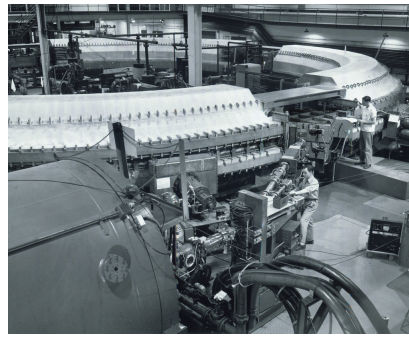


Fig. 8.2 Details of the low energy injection line and of the injection straight section at the Cosmotron

2442 8.1 Theory, Basic Concepts

2443 The synchrotron is based on two key principles: a varying magnetic field to maintain
 2444 the accelerated bunch on a constant orbit, with constant transverse focusing, namely,

$$B(t) = p(t)/q\rho, \quad \rho = \text{constant} \quad (8.1)$$

2445 and longitudinal phase stability, possibly including modulation of the accelerating
 2446 voltage frequency in order to follow the velocity change of the bunch [1, 2]. The
 2447 modulation of the oscillating voltage frequency is maintained in synchronism with
 2448 the bunch revolution motion, of which the period varies with time following

$$f_{RF}(t) = hf_{rev}(t) \quad (8.2)$$

2449 with h an integer, the “RF harmonic”. Since the orbit is maintained unchanged
 2450 turn after turn, the revolution frequency varies, in inverse proportion to particle
 2451 velocity. These are two major evolutions compared to the cyclotron, where, instead,
 2452 the magnetic field and the oscillating voltage frequency are fixed.

2453 The synchronism between RF voltage frequency and revolution time (Eq. 8.2)
 2454 allows maintaining the bunch at an appropriate phase, the “synchronous phase”, with
 2455 respect to the oscillating voltage when passing the accelerating gap (Fig. 8.18).

2456 Synchronous acceleration is technologically simpler in the case of electrons, as
 2457 frequency modulation is unnecessary beyond a few MeV of particle energy. For
 2458 instance, from $v/c = 0.9987$ at 10 MeV to $v/c \rightarrow 1$ at very high energy, the relative
 2459 change in revolution frequency amounts to $\delta f_{\text{rev}}/f_{\text{rev}} = \delta\beta/\beta < 0.0013$.

2460 Constant closed orbit reduces the radial extent of individual guiding magnets
 2461 compared to a cyclotron dipole which must encompass a spiraling orbit, and leads
 2462 to a circular string of dipoles, a ring structure. An archetype of a weak focusing syn-
 2463 chrotron ring is shown in Fig. 8.3, Saturne I, a 3 GeV, 4-period, 68.9 m circumference,
 2464 transverse index focusing synchrotron at Saclay [6]. Operation at Saturne I started in
 2465 1957, plans for the acceleration of polarized beams at the time motivated theoretical
 2466 investigation of resonant depolarization [7]. The four dipoles of the squared ring
 2467 are 1150 tons each; the straight sections are 4 m long; injection is in the north one
 2468 (foreground), from a 3.6 MeV Van de Graaff (not visible); the south section houses
 2469 the extraction system; a beam detection system is located in the east straight; the RF
 2470 cavity is in the west one and provides a peak voltage of a few kW, whereas the peak
 2471 power requested from the RF system for acceleration does not exceed 2 kW.

2472 For the sake of comparison: a synchro-cyclotron dipole is a pair of full, massive
 2473 cylindrical poles; greater energy requires greater radial extent of the magnet to allow
 2474 the necessary increase of the bend field integral (namely, $\oint B dl = 2\pi R_{\text{max}} \hat{B} =$
 2475 p_{max}/q - note that \hat{B} can be pushed to ~ 2 T as the field is fixed) and accordingly
 2476 of the diameter of the bulky cylinder, thus the volume of iron increases more than
 2477 quadratically with bunch rigidity.

2478 A second example of a weak focusing synchrotron is shown in Figure 8.4, the ZGS
 2479 at Argonne, a 12 GeV, 4-period, 172 m circumference, zero-gradient synchrotron:
 2480 ZGS had the particularity of using wedge focusing to ensure transverse beam sta-
 2481 bility. ZGS was operated over 1964-1979, polarized beam acceleration happened
 2482 in July 1973, to 8.5 GeV/c, and up to 12 GeV/c in the following years [8]. Pulsed
 2483 quadrupoles were used to pass through several depolarizing intrinsic resonances,
 2484 a method known as resonance crossing by fast “tune-jump”. ZGS proton injector
 2485 was comprised of a 20 keV source, followed by a 750 keV Cockcroft-Walton and a
 2486 50 MeV linac.

2487 The acceleration is cycled in a synchrotron, from injection to top energy, repeat-
 2488 edly. The cycling of the magnetic field, in synchronism with the acceleration voltage,
 2489 maintains a constant orbit; the field law $B(t)$ depends on the type of power supply. If
 2490 the ramping uses a constant electromotive force, then

$$B(t) \propto (1 - e^{-\frac{t}{\tau}}) = 1 - \left[1 - \left(\frac{t}{\tau}\right) + \left(\frac{t}{\tau}\right)^2 - \dots \right] \approx \frac{t}{\tau} \quad (8.3)$$

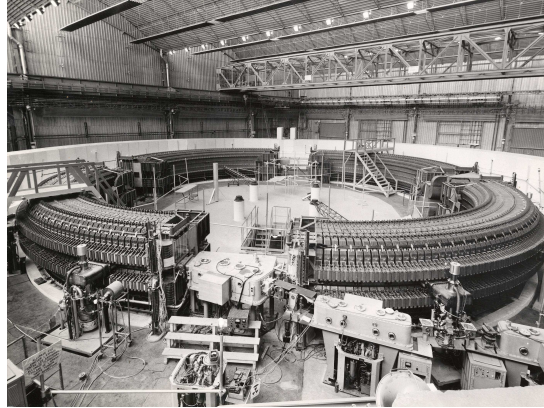


Fig. 8.3 Saturne I at Saclay [6], a 3 GeV, 4-period, 68.9 m circumference, weak focusing synchrotron, field index $n \approx 0.6$

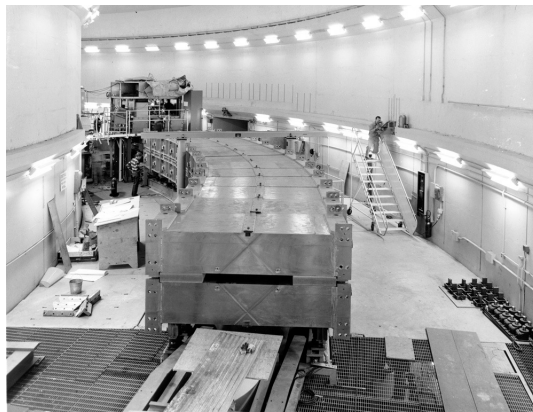


Fig. 8.4 The ZGS at Argonne during construction. A 12 GeV, 4-period, 172 m circumference, wedge focusing synchrotron. Two persons can be seen standing on the left and on the right of the ring, in the background, giving an idea of the size of the magnets

2491 essentially linear. In that case $\dot{B} = dB/dt$ does not exceed a few Tesla/second, thus
2492 the repetition rate of the acceleration cycle is of the order of a Hertz.

2493 If the magnet winding is part of a resonant circuit the field law has the form

$$B(t) = B_0 + \frac{\hat{B}}{2}(1 - \cos \omega t) \quad (8.4)$$

2494 so that, in the interval of half a voltage repetition period, namely $t : 0 \rightarrow \pi/\omega$,
2495 the field increases from an injection threshold value to a maximum value at highest
2496 rigidity, $B(t) : B_0 \rightarrow B_0 + \hat{B}$. The latter determines the highest achievable energy:
2497 $\hat{E} = pc/\beta = q\hat{B}\rho c/\beta$. The repetition rate with resonant magnet cycling can reach a
2498 few tens of Hertz.

2499 In both cases anyway B imposes its law and the other quantities comprising the
2500 acceleration cycle (RF frequency in particular) will follow B(t).

2501 For the sake of comparison again: in a synchrocyclotron the field is constant,
2502 acceleration can be cycled as fast as the voltage system allows; assume a conservative
2503 10 kVolts per turn, thus of the order of 10,000 turns to 100 MeV, with velocity

2504 $0.046 < v/c < 0.43$ from 1 to 100 MeV, proton. Take $v \approx 0.5c$ to make it simple,
 2505 an orbit circumference below 30 meter, thus the acceleration takes of the order of
 2506 $10^4 \times C/0.5c \approx \text{ms}$ range, potentially a repetition rate in kHz range, more than an
 2507 order of magnitude beyond what a rapid-cycling pulsed synchrotron allows.

2508 The next decades following the invention of the synchrotron saw an all-out break-
 2509 through, with applications in many fields of science, in medicine, industry. The
 2510 weak focusing synchrotron allowed colliding particle beams of highest energies on
 2511 fixed targets in nucleus fission and particle production experiments, leading to the
 2512 discovery of several fundamental particles. Its technological simplicity still makes
 2513 it an appropriate technology today in low energy beam application when relatively
 2514 low beam current is not a concern: it essentially requires a single type of a simple
 2515 dipole magnet, an accelerating gap, some command-control instrumentation, and
 2516 that's it! whereas it procures greater beam manipulation flexibilities compared to
 2517 (synchro-)cyclotrons.

2518 Transverse beam stability in a weak focusing synchrotron ring inherits from the
 2519 cyclotron techniques, focusing in the dipoles results from the presence of a transverse
 2520 field gradient $0 < n < 1$ and/or from wedge focusing, as in the aforementioned two
 2521 examples, Saturne 1 synchrotron [9] and the ZGS [10].

2522 A weak focusing synchrotron is comprised of a string of dipoles separated by
 2523 field free drift spaces, forming a $\frac{2\pi}{N}$ -symmetric, N-periodic structure. Each period
 2524 ensures a $\frac{2\pi}{N}$ fraction of the 2π bending. N=4 for instance in Saturne I (Fig. 8.3) and
 2525 in ZGS (Fig. 8.4). In the ZGS a period is comprised of a pair of 45 degree dipoles,
 2526 a total of 8 dipoles around the ring, whereas Saturne I features a single 90 degree
 2527 dipole per period, 4 dipoles in total.

2528 Introducing straight sections in the magnetic structure of the ring allows room
 2529 for inserting the various devices that garnish a synchrotron and contribute beam ma-
 2530 nipulation flexibility: an accelerating cavity, injection and extraction systems, beam
 2531 diagnostics equipment, special optical elements, tune jump quadrupoles possibly for
 2532 polarized beam handling, etc.

2533 8.1.1 Transverse Stability

2534 The introduction to transverse stability in this Section leans on basic concepts ad-
 2535 dressed in the Classical Cyclotron Chapter. Radial motion stability around a refer-
 2536 ence closed orbit in an axially symmetric dipole field requires the field configuration
 2537 sketched in Fig. 8.5: the magnetic rigidity $B \times \rho$ is an increasing function of ρ ,
 2538 $\frac{\partial B\rho}{\partial \rho} \geq 0$, viz. $1 + \frac{\rho}{B_0} \frac{\partial B}{\partial \rho} \geq 0$. Vertical stability requires the configuration sketched in
 2539 Fig. 8.6: the field decrease with radius, $\frac{\partial B_y}{\partial \rho} < 0$. This is the focusing method used in
 2540 the classical cyclotron, and has been discussed in Section 3.1.2. Introduce the field
 2541 index

$$n = -\frac{\rho_0}{B_0} \left. \frac{\partial B_y}{\partial \rho} \right|_{x=0, y=0} \quad (8.5)$$

2542 Transverse motion stability in an axially symmetric structure, with or without drift
 2543 spaces, thus summarizes in

$$0 < n < 1 \tag{8.6}$$

Fig. 8.5 Radial motion stability in an axially symmetric structure. The resultant $F_r = -qvB + mv^2/r$, is zero at I : $B_0\rho_0 = mv/q$. The resultant at i is toward I if $qvB_i < mv^2/\rho_i$, i.e. $B_i\rho_i < mv/q$; the resultant at e is toward I if $qvB_e > mv^2/\rho_e$, i.e. $B_e\rho_e > mv/q$

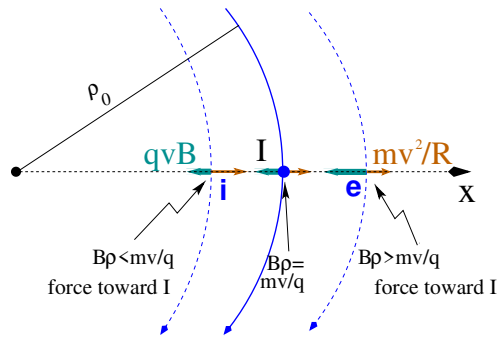
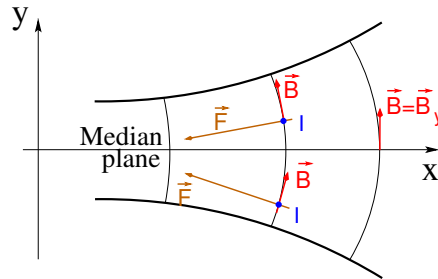


Fig. 8.6 Axial motion stability requires B to decrease with radius: the Laplace force pulls a charge at I (velocity pointing out of the page) toward the median plane. Increasing the field gradient increases the focusing



2544 Adding drift spaces requires defining two radii, namely,
 2545 (i) the magnet curvature radius ρ_0 (Fig. 8.7),
 2546 (ii) an average radius $R = C/2\pi = \rho_0 + Nl/\pi$ (with C the length of the reference
 2547 closed orbit and $2l$ the drift length) (Fig. 8.8) which also writes

$$R = \rho_0(1 + k), \quad k = \frac{Nl}{\pi\rho_0} \tag{8.7}$$

2548 The reference orbit is comprised of arcs of radius ρ_0 in the magnets, and straight
 2549 segments along the drift spaces that connect these arcs. Adding drift spaces decreases
 2550 the average focusing around the ring. Trajectories of different momenta are parallel.

Fig. 8.7 In a sector dipole with radial index $n \neq 0$, closed orbits follow arcs of constant B . A closed orbit at $p_0 + \Delta p$ follows an arc of radius $\rho_0 + \Delta\rho$, $\Delta\rho = \Delta p / (1 + n)qB_0$

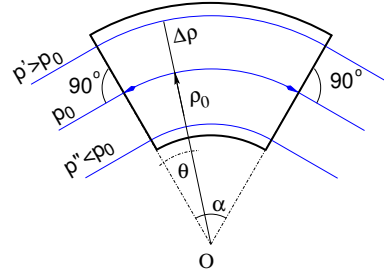
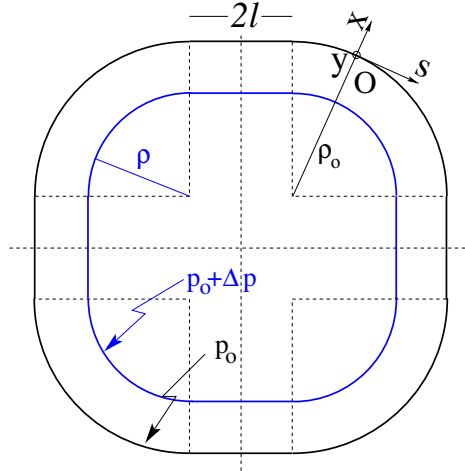


Fig. 8.8 A $2\pi/4$ axially symmetric structure with four drift spaces. Orbit length on reference momentum p_0 is $C = 2\pi\rho_0 + 8l$. $(O;s,x,y)$ is the moving frame, along the reference orbit. The orbit for momentum $p = p_0 + \Delta p$ ($\Delta p < 0$, here) is at constant distance $\Delta x = \frac{\rho_0}{1-n} \frac{\Delta p}{p_0} = \frac{R}{(1+k)(1-n)} \frac{\Delta p}{p_0}$ from the reference orbit



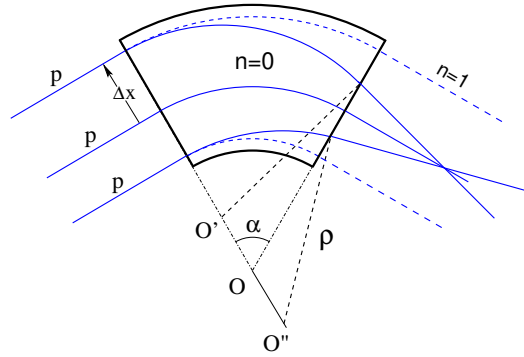
2551 *Geometrical focusing:*

2552 In a constant field dipole (radial field index $n=0$), the longer (respectively shorter)
 2553 path in the magnetic field for parallel trajectories entering the magnet at greater
 2554 (respectively smaller) radius results in geometrical focusing. Referring to Fig. 8.9,
 2555 this effect can be cancelled, *i.e.*, the deviation made the same whatever the entrance
 2556 radius, if the curvature center is made independent of the entrance radius: $OO' = 0$,
 2557 $O''O = 0$. This requires trajectories at an outer (inner) radius to experience a smaller
 2558 (greater) field so to satisfy $BL = B\rho\alpha = C^{st}$. Differentiating $B\rho = C^{st}$ yields
 2559 $\frac{\Delta B}{B} + \frac{\Delta\rho}{\rho} = 0$, with $\Delta\rho = \Delta x$. Thus the field $B(x)$ must satisfy $n = -\frac{\rho_0}{B_0} \frac{\Delta B}{\Delta x} = 1$ in
 2560 order to cancel the geometrical focusing resulting from the curvature.

2561 *Focal distance associated with the curvature:*

2562 Assume $n=0$, reference radius $\rho = \rho_0$, reference arc length $\mathcal{L} = \rho_0\alpha$. From $\frac{d^2x}{ds^2} +$
 2563 $\frac{1}{\rho_0^2}x = 0$ one gets

Fig. 8.9 Geometrical focusing: in a sector dipole with focusing index $n = 0$, parallel incoming rays of equal momenta experience the same curvature radius ρ , they exit converging, as a results of the longer path of outer trajectories in the field, compared to inner ones. An index value $n=1$ cancels that effect: rays exit parallel



$$\Delta x' = \int \frac{d^2x}{ds^2} ds \approx -\frac{x}{\rho_0^2} \int ds = -\frac{x}{\rho_0^2} \mathcal{L} \stackrel{def.}{=} -\frac{x}{f} \Rightarrow f = \frac{\rho_0^2}{\mathcal{L}} \quad (8.8)$$

2564 In a weak focusing structure ($0 < n < 1$) transverse motion stability is realized by
 2565 profiling the magnet gap (Fig. 8.6). A field index n close to 0 (parallel gap) enhances
 2566 radial focusing at the expense of axial focusing; n close to 1 enhances axial focusing
 2567 at the expense of radial focusing. Drawbacks of the method are, the weakness of the
 2568 focusing and the absence of independent radial and axial focusing.

2569 **Wedge Focusing**

2570 This is the focusing method in the ZGS. Profiling the magnet gap in order to adjust
 2571 the focal distance complicates the magnet; $n=0$, a parallel gap, makes it simpler.
 2572 In the ZGS the focal distance is designed based on proper entrance and exit wedge
 2573 angles (Fig. 8.10): opening the magnetic sector increases the horizontal focusing
 2574 (and decreases the vertical focusing); closing the magnetic sector has the reverse
 2575 effect.

2576 *Vertical focusing at the EFB*

2577 The magnetic field falls off smoothly in the fringe field region at the ends of a magnet,
 2578 from its value in the body to zero at some distance from the iron. The extent of the
 2579 fall-off is commensurate with the gap size, its shape depends on such factors as the
 2580 profiling of the iron at the EFB (Fig. 8.11) or the positioning and shape of the coils.

2581 From an optics standpoint, the main effect of the fringe field is the existence of a
 2582 longitudinal component of the field, $\mathbf{B}_s(s)$. In a mid-plane symmetry dipole, $\mathbf{B}_s(s)$
 2583 is non-zero off the median plane, and normal to the iron (Fig. 8.11).

2584 The focal distance f associated with a wedge angle ϵ (Fig. 8.10) satisfies

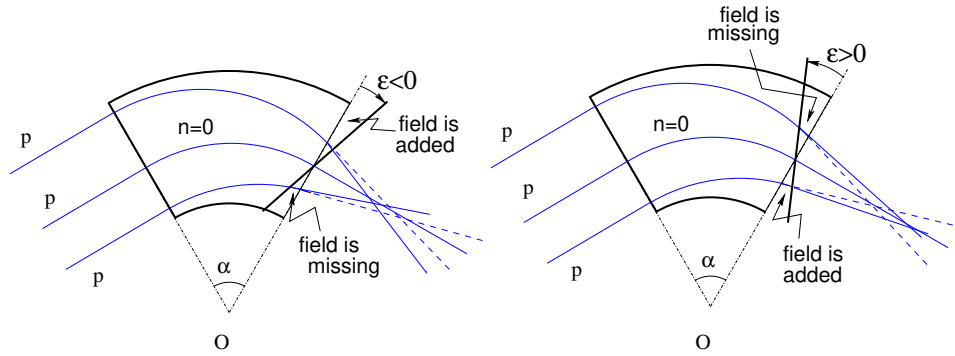


Fig. 8.10 Left: a focusing wedge ($\epsilon < 0$ by convention); opening the sector increases the horizontal focusing. Right: a defocusing wedge ($\epsilon > 0$ by convention); closing the sector decreases the horizontal focusing. The focal distance of the bend plane respectively decreases, increases. The effect is the opposite in the vertical plane, opening/closing the sector decreases/increases the vertical focusing.

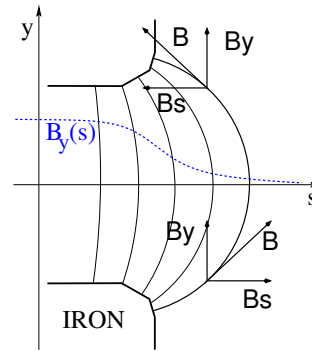


Fig. 8.11 Field components in the $B_y(s)$ fringe field region at a dipole EFB

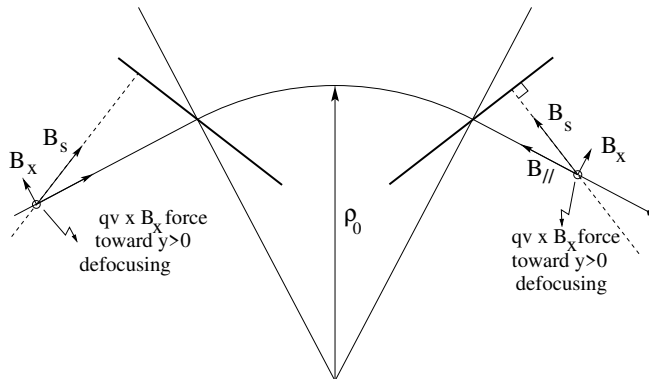


Fig. 8.12 Field components in the fringe field region at the end of a dipole ($y > 0$, here, referring to Fig. 8.11). $B_{//}$ is parallel to the particle velocity. This configuration is vertically defocusing: a charged particle traveling off mid-plane is pulled away from the latter under the effect of $\mathbf{v} \times \mathbf{B}_x$ force component. Inspection of the $y < 0$ region gives the same result: the charge is pulled away from the median plane

$$\frac{1}{f} = \tan \frac{\epsilon}{\rho_0} \quad (8.9)$$

2585 with $\epsilon > 0$ if the sector is closing, by convention. In a point transform approximation,
 2586 at the wedge the trajectory undergoes a local deviation proportional to the distance
 2587 to the optical axis, namely,

$$\Delta x' = \frac{\tan \epsilon}{\rho_0} \Delta x, \quad \Delta y' = -\frac{\tan \epsilon}{\rho_0} \Delta y \quad (8.10)$$

2588 Wedge vertical focusing in the ZGS ($\epsilon > 0$) was at the expense of horizontal
 2589 geometrical focusing (Fig. 8.7). This was an advantage though for the acceleration
 2590 of polarized beams, as radial field components (which are responsible for depolar-
 2591 ization) were only met at the EFBs of the eight main dipoles [8]. Preserving beam
 2592 polarization at high energy required tight control of the tunes, and this was achieved
 2593 by, in addition, pole face winding at the ends of the dipoles [11, 12]; these coils
 2594 where pulsed to control amplitude detuning, resulting in tune control at 0.01 level,
 2595 they also compensated eddy currents induced sextupole perturbations affecting the
 2596 vertical tune.

2597 *Fringe field extent*

2598 The fringe field extent, say λ , may be taken into account in the thin lens approximation
 2599 of the wedge focusing. It only modifies the horizontal focusing to the second order
 2600 in the coordinates, but changes the vertical focusing to the first order, namely

$$\Delta x' = \frac{\tan \epsilon}{\rho_0} \Delta x, \quad \Delta y' = -\frac{\tan(\epsilon - \psi)}{\rho_0} \Delta y \quad (8.11)$$

2601 wherein

$$\psi = I_1 \frac{\lambda}{\rho_0} \frac{1 + \sin^2 \epsilon}{\cos \epsilon}, \quad \text{with } I_1 = \int_{s(B=0)}^{s(B=B_0)} \frac{B(s)(B_0 - B(s))}{B_0^2} \frac{ds}{\lambda} \quad (8.12)$$

2602 and the integral I_1 extends over the field fall-off where B evolves between 0 to a
 2603 plateau value B_0 inside the magnet.

2604 **Off-momentum orbits**

In a dipole with field index $n = -\frac{\rho_0}{B_0} \frac{\partial B_y}{\partial \rho}$, concentric orbits with different momenta
 $p = p_0 + \Delta p$ (Fig. 8.7) are distant

$$\Delta x = \frac{\rho_0}{1 - n} \frac{\Delta p}{p_0}$$

2605 from the reference orbit at $p = p_0$ Given that $n < 1$,

2606 - higher momentum orbits, $p > p_0$, have a greater radius,

2607 - lower momentum orbits, $p < p_0$, have a smaller radius.

2608 In a structure with axial symmetry, with drift sections (Fig. 8.8) or without
 2609 (classical and AVF cyclotrons for instance), the ratio $\frac{\Delta x}{\rho_0 dp/p_0} = \frac{1}{1-n}$ is independent
 2610 of the azimuth s . Equilibrium trajectories enter and exit parallel to the optical axis
 2611 of the bending dipoles. Introduce the geometrical radius $R = (1+k)\rho_0$ (Eq. 8.7) to
 2612 account for the added drifts, the chromatic dispersion of the orbits thus amounts to

$$\frac{\Delta x}{\Delta p/p_0} \equiv \frac{\Delta R}{\Delta p/p_0} = \frac{R}{(1-n)(1+k)} \quad (8.13)$$

2613 Thus the dispersion function

$$D(s) = \frac{R}{(1-n)(1+k)} = D, \quad \text{constant} \quad (8.14)$$

2614 is s -independent, the distance of a chromatic orbit to the reference orbit is constant
 2615 around the ring.

2616 *Chromatic orbit length*

2617 In an axially symmetric structure the difference in closed orbit length $\Delta C = 2\pi\Delta R$
 2618 resulting from the difference in momentum arises in the dipoles, as all orbits are
 2619 parallel in the drifts (Fig. 8.8). Hence, from Eq. 8.13, the relative closed orbit
 2620 lengthening factor, “momentum compaction”

$$\alpha = \frac{\Delta C}{C} / \frac{\Delta p}{p_0} \equiv \frac{\Delta R}{R} / \frac{\Delta p}{p_0} = \frac{1}{(1-n)(1+k)} \approx \frac{1}{v_x^2} \quad (8.15)$$

with $k = Nl/\pi\rho_0$ (Eq. 8.7). A note regarding the relationship $\alpha \approx 1/v_x^2$ between mo-
 mentum compaction and horizontal wave number (it will be addressed quantitatively,
 below): this approximation was established in the case of a cylindrically symmetric
 structure, for which $v_x = \sqrt{1-n}$ (Eq. 3.22, ‘Classical Cyclotron’ Chapter). Adding
 short drifts such that $k \rightarrow 0$ (*i.e.*, $Nl \ll \pi\rho_0$), the relation still holds, thus leading to

$$v_x \approx \sqrt{(1-n)(1+k)} \approx \sqrt{(1-n)(1 + \frac{k}{2})}$$

2621 8.1.2 Betatron motion in a periodic structure, periodic stability

2622 Equations of motion

2623 The first order differential equations of motion in the Serret-Frénet frame (Fig. 8.8)
2624 derive from the Lorentz equation,

$$\frac{d\mathbf{mv}}{dt} = q\mathbf{v} \times \mathbf{B} \Rightarrow m \frac{d}{dt} \begin{Bmatrix} \frac{ds}{dt} \mathbf{s} \\ \frac{dx}{dt} \mathbf{x} \\ \frac{dy}{dt} \mathbf{y} \end{Bmatrix} = q \begin{Bmatrix} (\frac{dx}{dt} B_y - \frac{dy}{dt} B_x) \mathbf{s} \\ -\frac{ds}{dt} B_y \mathbf{x} \\ \frac{ds}{dt} B_x \mathbf{y} \end{Bmatrix} \quad (8.16)$$

2625 Introduce the field index $n = -\frac{\rho_0}{B_0} \frac{\partial B_y}{\partial x}$ evaluated on the reference orbit, with $B_0 =$
2626 $B_y(\rho_0, y = 0)$; assume transverse stability: $0 < n < 1$. Taylor expansion of the field
2627 components in the moving frame write

$$\begin{aligned} B_y(\rho) &= B_y(\rho_0) + x \left. \frac{\partial B_y}{\partial x} \right|_{\rho_0} + \mathcal{O}(x^2) \approx B_y(\rho_0) - n \frac{B_y}{\rho_0} \Big|_{\rho_0} x = B_0(1 - n \frac{x}{\rho_0}) \\ B_x(0 + y) &= \underbrace{B_x(0)}_{=0} + y \underbrace{\left. \frac{\partial B_x}{\partial y} \right|_{\rho_0}}_{= \frac{\partial B_y}{\partial x}} + (\text{higher order in } y) \approx -n \frac{B_0}{\rho_0} y \end{aligned} \quad (8.17)$$

2628 Introduce in addition $ds \approx v dt$, Eqs. 8.16, 8.17 lead to the differential equations of
2629 motion in a dipole field

$$\frac{d^2 x}{ds^2} + \frac{1-n}{\rho_0^2} x = 0, \quad \frac{d^2 y}{ds^2} + \frac{n}{\rho_0^2} y = 0 \quad (0 < n = \frac{\rho_0}{B_0} \frac{\partial B_y}{\partial x} < 1) \quad (8.18)$$

2630 It results that, in an S-periodic structure comprised of dipoles, wedges and drift
2631 spaces, the differential equation of motion takes the general form of Hill's equation, a
2632 second order differential equation with periodic coefficient, namely (with z standing
2633 for x or y),

$$\begin{cases} \frac{d^2 z}{ds^2} + K_z(s)z = 0 \\ K_z(s+S) = K_z(s) \end{cases} \quad \text{with} \quad \begin{cases} \text{in dipoles : } \begin{cases} K_x = (1-n)/\rho_0^2 \\ K_y = n/\rho_0^2 \end{cases} \\ \text{at a wedge : } K_y = \pm(\tan \epsilon)/\rho_0 \\ \text{in drift spaces : } K_x = K_y = 0 \end{cases} \quad (8.19)$$

2634 $K_z(s)$ is S-periodic, $S = 2\pi R/N$ ($S = C/4$, for instance, in the 4-periodic ring
2635 Saturne 1 (Figs. 8.3, 8.8)). G. Floquet has established [13] that the two independent
2636 solutions of Hill's second order differential equation have the form

$$\begin{cases} z_1(s) = \sqrt{\beta_z(s)} e^{i \int_0^s \frac{ds}{\beta_z(s)}} \\ dz_1(s)/ds = \frac{i - \alpha_z(s)}{\beta_z(s)} z_1(s) \end{cases} \quad \text{and} \quad \begin{cases} z_2(s) = z_1^*(s) \\ dz_2(s)/ds = dz_1^*(s)/ds \end{cases} \quad (8.20)$$

2637 wherein $\beta_z(s)$ and $\alpha_z(s) = -\beta'_z(s)/2$ are S-periodic functions, from what it results
2638 that

$$z_{\frac{1}{2}}(s+S) = z_{\frac{1}{2}}(s) e^{\pm i\mu_z} \quad (8.21)$$

2639 wherein

$$\mu_z = \int_{s_0}^{s_0+S} \frac{ds}{\beta_z(s)} \quad (8.22)$$

2640 is the betatron phase advance over a period. A real solution of Hill's equation is
 2641 the linear combination $A z_1(s) + A^* z_2^*(s)$. Take A of the form $A = \frac{1}{2} \sqrt{\epsilon/\pi} e^{i\phi}$
 2642 (the introduction of the constant multiplicative factor $\sqrt{\epsilon/\pi}$ is justified below), the
 2643 general solution of Eq. 8.19 then takes the form (noting $(*)' = d(*)/ds$)

$$\begin{cases} z(s) = \sqrt{\beta_z(s)\epsilon/\pi} \cos\left(\int \frac{ds}{\beta_z} + \phi\right) \\ z'(s) = -\sqrt{\frac{\epsilon/\pi}{\beta_z(s)}} \sin\left(\int \frac{ds}{\beta_z} + \phi\right) + \alpha_z(s) \cos\left(\int \frac{ds}{\beta_z} + \phi\right) \end{cases} \quad (8.23)$$

2644 The motion coordinates satisfy the following ellipse equation, Courant-Snyder in-
 2645 variant,

$$\frac{1}{\beta_z(s)} [z^2 + (\alpha_z(s)z + \beta_z(s)z')^2] = \frac{\epsilon}{\pi} \quad (8.24)$$

2646 At a given azimuth s of the periodic structure the observed turn-by-turn motion lies
 2647 on that ellipse (Fig. 8.13). The form of the ellipse depends on the observation azimuth
 2648 s via the respective local values of $\alpha_z(s)$ and $\beta_z(s)$, but its surface ϵ is invariant.
 2649 Motion along the ellipse is clockwise, as can be figured from Eq. 8.23 considering
 2650 an observation azimuth s where the ellipse is upright, $\alpha_z(s) = 0$.

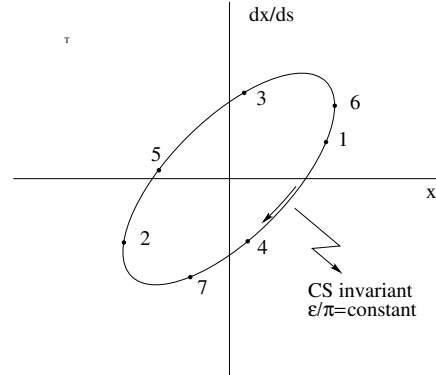


Fig. 8.13 Courant-Snyder invariant and turn-by-turn harmonic motion. The form of the ellipse depends on the observation azimuth s but its surface ϵ is invariant

2651 If a turn is comprised of N periods, the phase advance over a turn (from one
 2652 location to the next on the ellipse in Fig. 8.13) is

$$\int_{s_0}^{s_0+NS} \frac{ds}{\beta_z(s)} = N \int_{s_0}^{s_0+S} \frac{ds}{\beta_z(s)} = N\mu_z \quad (8.25)$$

2653 *Weak focusing approximation*

In the case of a cylindrically symmetric structure, a sinusoidal motion (Eqs. 3.15, 3.16, “Classical Cyclotron” Chapter) is the exact solution of the first order differential equations of motion. In that case the latter have a constant (s-independent) coefficient, $K_x = (1 - n)/R_0^2$ and $K_y = n/R_0^2$, respectively. Adding drift spaces results in Hill’s differential equation with periodic coefficient $K(s + S) = K(s)$ (Eq. 8.19) and to a pseudo harmonic solution (Eq. 8.23). Due to the weak focusing the beam envelope (Eq. 8.30) is only weakly modulated, thus so is $\beta_z(s)$. In a practical manner, the modulation of $\beta_z(s)$ does not exceed a few percent, this justifies introducing the average value $\bar{\beta}_z$ to approximate the phase advance by

$$\int_0^s \frac{ds}{\beta_z(s)} \approx \frac{s}{\bar{\beta}_z} = v_z \frac{s}{R}$$

2654 The right equality is obtained by applying this approximation to the the phase advance
2655 per period (Eq. 8.32), namely $\mu_z = \int_{s_0}^{s_0+S} \frac{ds}{\beta_z(s)} \approx S/\bar{\beta}_z$, and introducing the wave
2656 number of the N-period optical structure

$$v_z = \frac{N\mu_z}{2\pi} = \frac{\text{phase advance over a turn}}{2\pi} \quad (8.26)$$

2657 so that

$$\bar{\beta}_z = \frac{R}{v_z} \quad (8.27)$$

2658 Substituting in Eq. 8.23 results in the approximate solution

$$\begin{cases} z(s) \approx \sqrt{\beta_z(s)\epsilon/\pi} \cos\left(v_z \frac{s}{R} + \phi\right) \\ z'(s) = -\sqrt{\frac{\epsilon/\pi}{\beta_z(s)}} \sin\left(v_z \frac{s}{R} + \phi\right) + \alpha_z(s) \cos\left(v_z \frac{s}{R} + \phi\right) \end{cases} \quad (8.28)$$

2659 In this approximation, the differential equations of motion (Eq. 8.19) can be
2660 expressed under the form

$$\frac{d^2x}{ds^2} + \frac{v_x^2}{R^2}x = 0, \quad \frac{d^2y}{ds^2} + \frac{v_y^2}{R^2}y = 0 \quad (8.29)$$

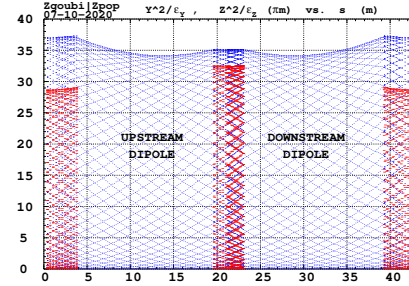
2661 *Beam envelopes*

2662 The beam envelope $\hat{z}(s)$ (with z standing for x or y) is determined by the particle of
2663 maximum invariant ϵ/π , it is given by

$$\pm \hat{z}(s) = \pm \sqrt{\beta_z(s)\epsilon/\pi} \quad (8.30)$$

As $\beta_z(s)$ is S-periodic, so is the envelope, $\hat{z}(s + S) = \hat{z}(s)$. In a cell with symmetries

Fig. 8.14 ***** rem-
place par envelope in saturne1
***** Beam envelope
along Saturne I four cells,
generated by a single particle
over many turns. The extreme
excursion at any azimuth s
tangents the envelope. En-
velopes along a cell feature
central symmetry, as does the
cell



2664
2665 (for instance symmetry with respect to the center of the cell), the envelope features
2666 the same symmetries. Envelope extrema are at azimuth s where $\beta_z(s)$ is minimum,
2667 or maximum, *i.e.*, where $\alpha_z = 0$ as $\beta'_z = -2\alpha_z$. This is illustrated in Fig. 8.14. No
2668 particular hypothesis regarding the amplitude of the motion is required here, it does
2669 not have to be paraxial and can be arbitrarily large (as long as transverse stability
2670 still holds).

2671 In the paraxial approximation, envelopes along the optical structure can be deter-
2672 mined by resorting to matrix transport (*cf.* reminders in Section 18.3.2). An initial
2673 beam matrix at some azimuth s , as well as the phase advance over a period, can
2674 be obtained using the stability criterion (Eq. 18.3.3). This is a simple exercise in
2675 the case of Saturne I type of structure (Figs. 8.3, 8.8). The transport matrix of the
2676 symmetric drift-dipole-drift cell satisfies

$$\begin{aligned}
 [T_{\text{per.}}] &= \begin{bmatrix} 1 & l \\ 0 & 1 \end{bmatrix} \begin{bmatrix} \cos(\sqrt{K_z}\rho_0\alpha) & \frac{1}{\sqrt{K_z}} \sin(\sqrt{K_z}\rho_0\alpha) \\ -\sqrt{K_z} \sin(\sqrt{K_z}\rho_0\alpha) & \cos(\sqrt{K_z}\rho_0\alpha) \end{bmatrix} \begin{bmatrix} 1 & l \\ 0 & 1 \end{bmatrix} \\
 &= \begin{bmatrix} \cos(\sqrt{K_z}\rho_0\alpha) - \sqrt{K_z}l \sin(\sqrt{K_z}\rho_0\alpha) & 2l \cos(\sqrt{K_z}\rho_0\alpha) + \frac{1}{\sqrt{K_z}} \sin(\sqrt{K_z}\rho_0\alpha)(1 - K_z l^2) \\ -\sqrt{K_z} \sin(\sqrt{K_z}\rho_0\alpha) & \cos(\sqrt{K_z}\rho_0\alpha) - \sqrt{K_z}l \sin(\sqrt{K_z}\rho_0\alpha) \end{bmatrix} \\
 &\approx \begin{bmatrix} \cos \sqrt{K_z}(\rho_0\alpha + l) & 2l \cos(\sqrt{K_z}\rho_0\alpha) + \frac{1}{\sqrt{K_z}} \sin(\sqrt{K_z}\rho_0\alpha) \\ -\sqrt{K_z} \sin(\sqrt{K_z}\rho_0\alpha) & \cos \sqrt{K_z}(\rho_0\alpha + l) \end{bmatrix} \quad (8.31)
 \end{aligned}$$

2677 The approximation is obtained by assuming that the drift length $2l$ is small compared
2678 to the arc length $\rho_0\alpha$. From the stability criterion $[T_{\text{per.}}] = I \cos \mu_z + J \sin \mu_z$ it results
2679 that $\frac{1}{2}\text{Tr}[T_{\text{per.}}] = \cos \mu_z$, which yields the phase advance

$$\mu_z = \sqrt{K_z}(\rho_0\alpha + l) = \sqrt{K_z}\rho_0\alpha(1 + k/2) \quad (8.32)$$

2680 With $\nu_z = N\mu_z/2\pi$ and (Eq. 8.19) $K_x = (1 - n)/\rho_0^2$, $K_y = n/\rho_0^2$, $N\alpha = 2\pi$,
2681 $k = 2l/\rho_0\alpha \ll 1$, this yields for the horizontal and vertical tunes

$$v_x \approx \sqrt{1-n}\left(1 + \frac{k}{2}\right) \approx \sqrt{(1-n)\frac{R}{\rho_0}}, \quad v_y \approx \sqrt{n}\left(1 + \frac{k}{2}\right) \approx \sqrt{n\frac{R}{\rho_0}} \quad (8.33)$$

2682 The identification $[T_{\text{per.}}] = I \cos \mu_z + J \sin \mu_z$ allows writing $[T_{\text{per.}}]$ under the
2683 form

$$[T_{\text{per.}}] = \begin{bmatrix} \cos \sqrt{K_z}(\rho_0 \alpha + l) & \frac{1 + \sqrt{K_z} l \cot(\sqrt{K_z} \rho_0 \alpha)}{\sqrt{K_z}} \sin \sqrt{K_z}(\rho_0 \alpha + l) \\ -\frac{\sqrt{K_z}}{1 + \sqrt{K_z} l \cot(\sqrt{K_z} \rho_0 \alpha)} \sin \sqrt{K_z}(\rho_0 \alpha + l) & \cos \sqrt{K_z}(\rho_0 \alpha + l) \end{bmatrix} \quad (8.34)$$

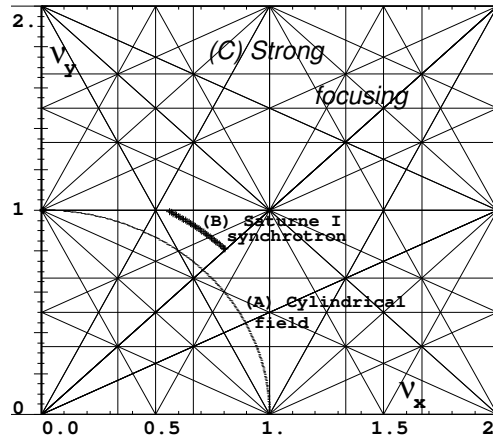
2684 so leading to the optical functions at the center of the drift,

$$\alpha_z = 0, \quad \beta_z = \frac{1}{\sqrt{K_z}} \left[1 + \sqrt{K_z} l \cot(\sqrt{K_z} \rho_0 \alpha) \right] \quad (8.35)$$

2685 Stability diagram

2686 The “working point” of the synchrotron is the couple (v_x, v_y) at which the acceler-
2687 ator is operated, it fully characterizes the focusing. In a structure with cylindrical
2688 symmetry (*cf.* Eq. 3.17) $v_x = \sqrt{1-n}$ and $v_y = \sqrt{n}$ so that $v_x^2 + v_y^2 = 1$: when the
2689 radial field index n is changed the working point stays on a circle of radius 1 in the
stability diagram (or “tune diagram”, Fig. 8.15). If drift spaces are added, in a first

Fig. 8.15 Location of the working point in the tune diagram, in case of (A) field with revolution symmetry, on a circle of radius 1; (B) sector field with index + drift spaces, on a circle of radius $(\sqrt{R/\rho_0})$; (C) strong focusing, $(|n| \gg 1)$, in large v_x, v_y regions.



2690 approximation (Eq. 8.33)
2691

$$v_x = \sqrt{(1-n)\frac{R}{\rho_0}}, \quad v_y = \sqrt{n\frac{R}{\rho_0}}, \quad v_x^2 + v_y^2 = \frac{R}{\rho_0} \quad (8.36)$$

2692 the working point is located on the circle of radius $\sqrt{R/\rho_0} > 1$.

Horizontal and vertical focusing are not independent: if ν_x increases then ν_y decreases and reciprocally; none can exceed the limits

$$0 < \nu_{x,y} < \sqrt{R/\rho_0}$$

2693 This is a lack of flexibility which strong focusing will overcome by providing two
2694 knobs so allowing adjustment of both tunes separately.

2695 8.1.3 Longitudinal Motion

2696 Acceleration of the Ideal Particle

2697 In a synchrotron, the field B is varied (a function performed by the power supply)
2698 as well as the bunch momentum p (a function performed by the accelerating cavity)
2699 in such a way that at any time $B(t)\rho = p(t)/q$ (ρ is the curvature radius of the
2700 central trajectory in the bending magnets). If this condition is fulfilled, then at all
2701 times during the acceleration cycle the central trajectory remains on the design
2702 optical axis, which is comprised of the reference arc in the dipoles, of the axis of
2703 the vacuum pipe in the straight section, of the accelerating cavities, of the beam
2704 position monitors, etc. Given the energies involved, the magnet supply imposes its
2705 law and the cavity follows $B(t)$, the best in can. A schematic $B(t)$ law is represented
in Fig. 8.16.

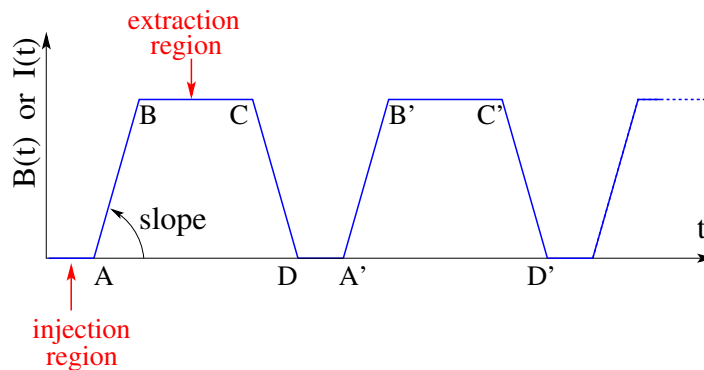


Fig. 8.16 Cycling $B(t)$ in a pulsed synchrotron. Ignoring saturation, $B(t)$ is proportional to the magnet power supply current $I(t)$. Bunch injection occurs at low field, in the region of A, extraction occurs at top energy, on the high field plateau. (AB): field ramp up (acceleration); (BC): flat top (includes beam extraction period); (CD): field ramp down; (DA'): thermal relaxation. (AA'): repetition period; $(1/AA')$: repetition rate; *slope*: ramp velocity $\dot{B} = dB/dt$ (Tesla/s).

2706

Typical values from Saturne I synchrotron are given in Tab. 8.1. As the central

Table 8.1 Saturne I field parameters

\dot{B}	1.8 T/s
B_{\max}	1.5 T
ρ	8.42 m
$B_{\max}\rho$	13 T m

trajectory length is fixed ($2\pi R \approx 68.9$ m, see Tab. 8.2) whereas particle velocity increases turn after turn, thus the revolution time T_{rev} varies.

$$T_{\text{rev}} = \frac{\text{duration of a turn}}{\text{velocity}} = \frac{2\pi R}{\beta c}$$

$$R_{\text{Sat.I}} = 10.97 \text{ m}, \begin{cases} \text{initial E} = 3.6 \text{ MeV} \\ \text{final E} = 2.94 \text{ GeV} \end{cases} \Rightarrow \begin{cases} T_{\text{rev}} = \frac{2\pi R}{0.09 \times 3 \times 10^8} = 16.5 \mu\text{s}; f = 0.06 \text{ MHz} \\ T_{\text{rev}} = \frac{2\pi R}{0.97 \times 3 \times 10^8} = 0.24 \mu\text{s}; f = 4.2 \text{ MHz} \end{cases}$$

The accelerating voltage $\hat{V}(t) = \sin \omega_{\text{rf}} t$ (Fig. 8.18) is maintained in synchronism with the revolution motion, thus its angular frequency ω_{rf} follows $h f_{\text{rev}}$,

$$\omega_{\text{rf}} = h\omega_{\text{rev}} = h \frac{c}{R} \frac{B(t)}{\sqrt{\left(\frac{m_0}{q\rho}\right)^2 + B^2(t)}}$$

2707 Energy gain

2708 The variation of the particle energy over a turn amounts to the work of the force
2709 $F = dp/dt$ on the charge at the cavity, namely

$$\Delta W = F \times 2\pi R = 2\pi q R \rho \dot{B} \quad (8.37)$$

Over most of the acceleration cycle in a slow-cycling synchrotron \dot{B} is usually constant (Eq. 8.3), thus so is ΔW . At Saturne I for instance

$$\frac{\Delta W}{q} = 2\pi R \rho \dot{B} = 68.9 \times 8.42 \times 1.8 = 1044 \text{ volts}$$

The field ramp lasts

$$\Delta t = (B_{\max} - B_{\min})/\dot{B} \approx B_{\max}/\dot{B} = 0.8 \text{ s}$$

The number of turns to the top energy ($W_{\max} \approx 3 \text{ GeV}$) is

$$N = \frac{W_{\max}}{\Delta W} = \frac{3 \times 10^9 \text{ eV}}{1044 \text{ eV}} \approx 3 \times 10^6$$

2710 **Adiabatic damping of betatron oscillations**

During acceleration, focusing strengths follow the increase of particle rigidity, so to maintain the tunes ν_x and ν_y constant. As a result of the longitudinal acceleration at the cavity though, the longitudinal energy of the particles is modified. This results in a decrease of the amplitude of betatron oscillations (an increase if the cavity is decelerating). The mechanism is sketched in Fig. 8.17: the slope, respectively before (index 1) and after (index 2) the cavity is

$$\frac{dx}{ds} = \frac{m \frac{dx}{dt}}{m \frac{ds}{dt}} = \frac{p_x}{p_s}, \quad \frac{dx}{ds} \Big|_2 = \frac{m \frac{dx}{dt}}{m \frac{ds}{dt}} \Big|_2 = \frac{p_{x,2}}{p_{s,2}}$$

Particle mass and velocity are modified at the traversal of the cavity but, as the

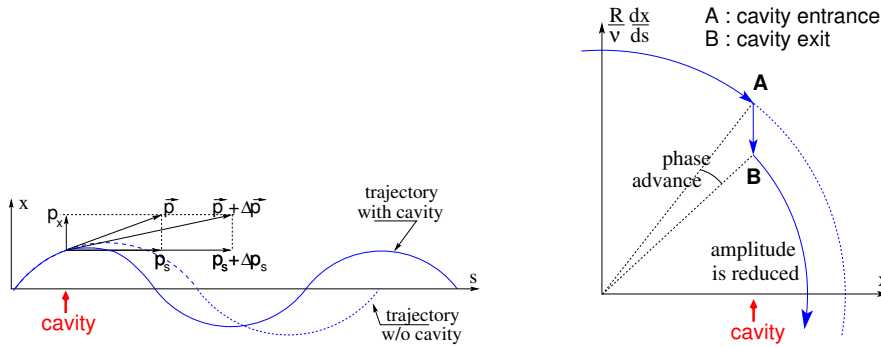


Fig. 8.17 Adiabatic damping of betatron oscillations, here from $x' = p_x/p_s$ before the cavity, to $x'_2 = p_x/(p_s + \Delta p_s)$ after the cavity. In the horizontal phase space, to the right, decrease of $\Delta \left(\frac{dx}{ds} \right)$ if $\frac{dx}{ds} > 0$, increase of $\Delta \left(\frac{dx}{ds} \right)$ if $\frac{dx}{ds} < 0$

force is longitudinal, $dp_x/dt = 0$ thus $p'_x = p_x$, the increase in momentum is purely longitudinal, $p'_s = p_s + \Delta p$. Thus

$$\frac{dx}{ds} \Big|_2 = \frac{p_x}{p_s + \Delta p} \approx \frac{p_x}{p_s} \left(1 - \frac{\Delta p}{p_s} \right)$$

and as a consequence the slope dx/ds varies across the cavity,

$$\Delta \left(\frac{dx}{ds} \right) = \frac{dx}{ds} \Big|_2 - \frac{dx}{ds} = - \frac{dx}{ds} \frac{\Delta p_s}{p_s}$$

2711 The slope varies in proportion to the slope, with opposite sign if $\Delta p/p > 0$ (accel-
2712 eration) thus a decrease of the slope. This variation has two consequences on the
2713 betatron oscillation (Fig. 8.17):

2714 - a change of the betatron phase,

2715 - a modification of the betatron amplitude.

2716 *In matrix form*

2717 Coordinate transport through the cavity writes $\begin{cases} x_2 = x \\ x_2' \approx \frac{p_x}{p_s}(1 - \frac{dp}{p}) = x'(1 - \frac{dp}{p}) \end{cases}$,

2718 hence the transfer matrix of the cavity,

$$[C] = \begin{bmatrix} 1 & 0 \\ 0 & 1 - \frac{dp}{p} \end{bmatrix} \quad (8.38)$$

2719 its determinant is $1 - dp/p \neq 1$: the system is non-conservative (the surface in phase
2720 space is not conserved). Assume one cavity in the ring and not $[T] \times [C]$ the one-turn
2721 matrix with origin at entrance of the cavity. Its determinant is $\det[T] \times \det[C] =$
2722 $\det[C] = 1 - \frac{dp}{p}$. Over N turns the coordinate transport matrix is $([T][C])^N$, its
2723 determinant is $(1 - \frac{dp}{p})^N \approx 1 - N\frac{dp}{p}$. The surface of the beam ellipse is $\epsilon \times$
2724 $\det[T]_{turn} = \epsilon_0 - \epsilon \frac{dp}{p}$ thus $\frac{d\epsilon}{\epsilon} = -\frac{dp}{p}$, the solution of which is

$$\epsilon \times p = \text{constant, or } \beta\gamma\epsilon = \text{constant} \quad (8.39)$$

2725 **Synchrotron motion; the synchronous particle**

2726 By “synchrotron motion”, or “phase oscillations”, it is meant a mechanism that
2727 stabilizes the longitudinal motion of a particle around a synchronous phase, in virtue
2728 of

- 2729 (i) the presence of a cavity with its frequency indexed on the revolution time,
- 2730 (ii) with the bunch centroid positioned either on the rising slope of the oscillating
2731 voltage (low energy regime), or on the falling slope (high energy regime).

The synchronous (or “ideal”) particle follows the equilibrium trajectory around the ring (the reference closed orbit, about which all other particles will undergo a betatron oscillation) and its velocity satisfies

$$B\rho = \frac{p}{q} = \frac{mv}{p} \rightarrow v = \frac{qB\rho}{m}$$

- 2732 - the revolution time is $T_{rev} = \frac{2\pi R}{v} = \frac{2\pi R}{\beta c} = \frac{2\pi R}{qB\rho/m}$
- the angular revolution frequency follows the increase of B:

$$\omega_{rev} = \frac{2\pi}{T_{rev}} = \frac{qB\rho}{mR}$$

- 2733 - during the acceleration $B(t)$ increases at a $\frac{dB}{dt} = \dot{B}$ rate normally of the order of a
2734 Tesla/second.

- in order for the ideal particle to stay on the closed orbit during the acceleration, its changing momentum must at all time satisfy $B(t)\rho = p(t)/q$. This defines $p(t)$ as a function of $B(t)$, and the following B dependence of mass and angular frequency:

$$m(t) = \gamma(t)m_0 = \frac{q\rho}{c} \sqrt{\left(\frac{m_0}{qc\rho}\right)^2 + B(t)^2}$$

$$\omega_{rev}(t) = \frac{c}{R} \frac{B(t)}{\sqrt{\left(\frac{m_0}{qc\rho}\right)^2 + B(t)^2}}$$

2735 - the RF voltage frequency $\omega_{RF}(t) = h\omega_{rev}(t)$ follows B(t), this maintains the
2736 synchronous phase at a fixed value

2737 - over a turn the gain in energy is $\Delta W = 2\pi qR\rho\dot{B}$, the reference particle experiences
2738 a voltage $V = \Delta W/q = 2\pi R\rho\dot{B}$.

2739 Simulation wise, the ramping of the guide field can be assumed to follow a step
2740 function in correlation with the step increase of particle momentum at the RF cavity.

2741 In that manner, the synchronous particle is maintained on the design orbit, at radius
2742 $\rho = p(t)/qB(t)=\text{constant}$ in the guide magnets.

2743 *Phase stability*

2744 Note ϕ_s the RF phase at arrival of the synchronous particle at the cavity. Its energy
2745 gain is $\Delta W = q\hat{V} \sin \phi_s = 2\pi qR\rho\dot{B} \cdot |\sin \phi_s| < 1$ imposes a lower limit to the cavity
2746 voltage for acceleration to happen, namely $\hat{V} > 2\pi R\rho\dot{B}$.

2747 The synchronous phase can be placed on the left (A A' A''... series in Fig. 8.18)
2748 or on the right (B B' B''... series) of the oscillating voltage crest. One and only
2749 one of these two possibilities, and which one depends on the optical lattice and on
2750 particle energy, ensures that particles in a bunch remain grouped in the vicinity of
2751 the synchronous particles. The transition between these two regimes (A series or B
2752 series) occurs at the transition γ , γ_{tr} , a property of the lattice. If the bunch energy
2753 is below transition energy, $E_{\text{bunch}} < m\gamma_{tr}$, the bunch has to present itself on the
2754 left of the crest (A series), if the bunch energy is greater than transition energy,
2755 $E_{\text{bunch}} > m\gamma_{tr}$, the bunch has to present itself on the right of the crest (B series).

2756 *Transition energy*

2757 The transition between the two regimes occurs at $\frac{dT_{rev}}{T_{rev}} = 0$. With $T = 2\pi/\omega = C/v$,

2758 this can be written $\frac{d\omega_{rev}}{\omega_{rev}} = -\frac{dT_{rev}}{T_{rev}} = \frac{dv}{v} - \frac{dC}{C}$. With $\frac{dv}{v} = \frac{1}{\gamma^2} \frac{dp}{p}$ and momentum

2759 compaction $\alpha = \frac{dC}{C} / \frac{dp}{p}$, (Eq. 8.15), this can be written

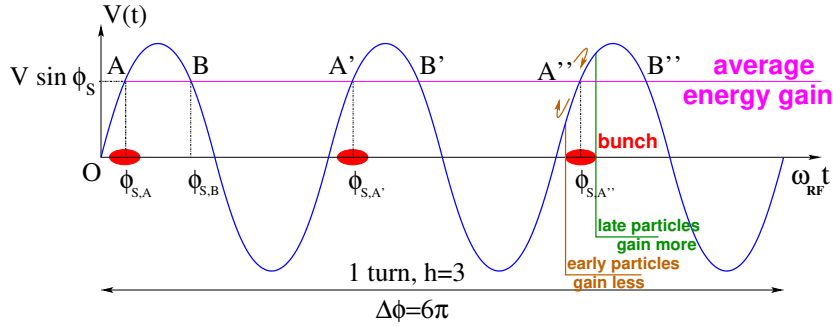


Fig. 8.18 Mechanism of phase stability, “longitudinal focusing”. Below transition ($\gamma < \gamma_{tr}$) phase stability occurs for a synchronous phase taken at either of the $h=3$ stable locations A, A', A'': a particle with higher energy goes around the ring more rapidly than the synchronous particle, it arrives earlier at the voltage gap (at $\phi < \phi_{s,A}$) and experiences a lower voltage; at lower energy the particle is slower, it arrives at the gap later compared to the synchronous particle, at $\phi > \phi_{s,A}$, and experiences a greater voltage; this results overall in a stable oscillatory motion around the synchronous phase. Beyond transition ($\gamma > \gamma_{tr}$) the stable phase is at either of the $h=3$ stable locations B, B', B'': a particle which is less energetic than the synchronous particle arrives earlier, $\phi < \phi_{s,B}$, it experiences a greater voltage, and inversely when it eventually gets more energetic than the synchronous particle

$$\frac{d\omega_{rev}}{\omega_{rev}} = -\frac{dT_{rev}}{T_{rev}} = \left(\frac{1}{\gamma^2} - \alpha\right) \frac{dp}{p} = \eta \frac{dp}{p} \tag{8.40}$$

2760 wherein the phase-slip factor has been introduced,

$$\eta = \overbrace{\frac{1}{\gamma^2}}^{\text{kinematics}} - \underbrace{\alpha}_{\text{lattice}} \tag{8.41}$$

2761 In a weak focusing structure $\alpha \approx 1/\nu_x^2$ (Eqs. 3.22, 8.15), thus the phase stability
2762 regime is

$$\text{below transition, i.e. } \phi_s < \pi/2, \quad \text{if } \gamma < \nu_x \tag{8.42}$$

$$\text{above transition, i.e. } \phi_s > \pi/2, \quad \text{if } \gamma > \nu_x \tag{8.43}$$

$$\tag{8.44}$$

2763 In weak focusing synchrotrons the horizontal tune $\nu_x = \sqrt{(1-n)R/\rho_0}$ (Eq. 8.33)

2764 may be ≥ 1 , and subsequently $\gamma_{tr} \approx \nu_x \geq 1$ depending on the horizontal tune value.

2765 Saturne I for instance, with $\nu_x \approx 0.7$ (Tab. 8.2), operated above transition energy.

2766 8.1.4 Spin Motion, Depolarizing Resonances

2767 The availability of polarized proton sources allowed the acceleration of polarized
 2768 beams to high energy. The possibility was considered from the early times of the
 2769 ZGS [14], up to 70% polarization transmission through the synchrotron was fore-
 2770 seen, polarization manipulation concepts included harmonic orbit correction, tune
 2771 jump at strongest depolarizing resonances (Fig. 8.19). Acceleration of a polarized
 2772 proton beam happened for the first time in a synchrotron and to multi-GeV energy in
 2773 1973, four years after the ZGS startup. Beams were accelerated up to 17 GeV with
 2774 substantial polarization maintained [8]. Experiments were performed to assess the
 2775 possibility of polarization transmission in strong focusing synchrotrons, and polar-
 2776 ization lifetime in colliders [15]. Acceleration of polarized deuteron was achieved in
 2777 the late 1970s, when sources were made available [16].

2778 The field index is essentially zero in the ZGS, transverse focusing is ensured
 2779 by wedge angles at the ends of the height dipoles, which is thus the only location
 2780 where non-zero horizontal field components are found. The vertical wave number
 2781 is small in addition, less than 1. This results in depolarizing resonance strengths
 2782 on the weak side, “As we can see from the table, the transition probability [from
 2783 spin state $\psi_{1/2}$ to spin state $\psi_{-1/2}$] is reasonably small up to $\gamma = 7.1$ ” [8], i.e.
 2784 $G\gamma = 12.73$, $p = 6.6$ GeV/c; the table referred to stipulates a transition probability
 2785 $P_{\frac{1}{2},-\frac{1}{2}} < 0.042$, whereas resonances beyond that energy range feature $P_{\frac{1}{2},-\frac{1}{2}} > 0.36$.
 2786 Beam depolarization up to 6 GeV/c, under the effect of these resonances, is illustrated
 2787 in Fig. 8.19.

2788 In weak focusing synchrotron particles experience radial fields all along the
 2789 bend dipoles as an effect of the radial field index, as they undergo vertical betatron
 2790 oscillations. However these radial field components are weak, and so is their effect
 2791 on spin motion, as long as the particle energy (the γ factor in the spin precession
 2792 equation) is not too high.

Assuming a defect-free ring, the vertical betatron motion excites “intrinsic” spin resonances, located at

$$G\gamma_R = kP \pm \nu_y$$

with k an integer and P the period of the ring. In the ZGS for instance, $\nu_y \approx 0.8$
 (Tab. 8.3), the ring $P=4$ -periodic, thus $G\gamma_R = 4k \pm 0.8$. Strongest resonances are
 located at

$$G\gamma_R = MPk \pm \nu_y$$

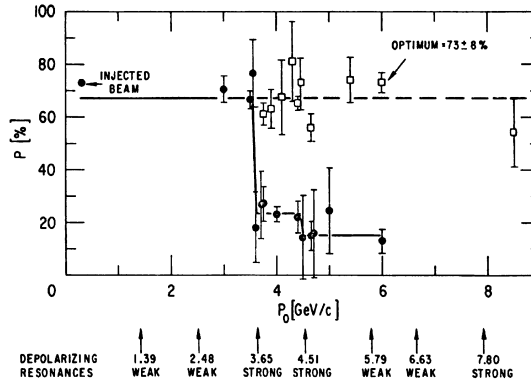
2793 with M the number of cells per superperiod [17, Sec. 3.II]. In the ZGS, $M=2$ thus
 2794 strongest resonances occur at $G\gamma_R = 2 \times 4k \pm 0.8$.

In the presence of vertical orbit defects, non-zero periodic transverse fields are ex-
 perimented along the closed orbit, they excite “imperfection” depolarizing resonances,
 located at

$$G\gamma_R = k$$

with k an integer. In the case of systematic defects the periodicity of the orbit is
 that of the lattice, P , imperfection resonances are located at $G\gamma_R = kP$. Strongest

Fig. 8.19 Depolarizing intrinsic resonance landscape up to 6 GeV/c at the ZGS (solid circles). Systematic resonances are located at $G\gamma_R = 4 \times \text{integer} \pm \nu_y$, strongest ones at $G\gamma_R = 8 \times \text{integer} \pm \nu_y$. Tune jump was used to preserve polarization when crossing strong resonances (empty circles) [18]



imperfection resonances are located at

$$G\gamma_R = MPk$$

2795 with M the number of cells per superperiod [17, Sec. 3.II]. Crossing a depolarizing
 2796 resonance, during acceleration, causes a loss of polarization given by (Froissart-Stora
 2797 formula [7])

$$\frac{P_f}{P_i} = 2e^{-\frac{\pi}{2} \frac{|\epsilon_R|^2}{\alpha}} - 1 \quad (8.45)$$

2798 from a value P_i upstream to an asymptotic value P_f downstream of the resonance.
 2799 This assumes an isolated resonance, passed with a crossing speed

$$\alpha = G \frac{d\gamma}{d\theta} = \frac{1}{2\pi} \frac{\Delta E}{M} \quad (8.46)$$

2800 with ΔE the energy gain per turn and M the mass. ϵ_R is the resonance strength.

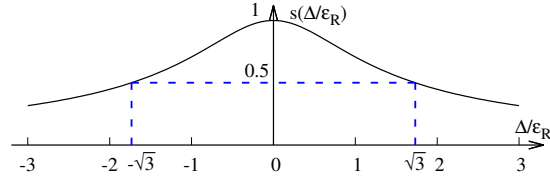
2801 *Spin precession axis. Resonance width*

2802 Consider the spin vector $\mathbf{S}(\theta) = (S_\eta, S_\xi, S_y)$ of a particle in the laboratory frame,
 2803 with θ the orbital angle around the accelerator. Introduce the projection $s(\theta)$ of \mathbf{S}
 2804 in the median plane

$$s(\theta) = S_\eta(\theta) + jS_\xi(\theta) \quad (\text{and } S_y^2 = 1 - s^2) \quad (8.47)$$

2805 It can be shown that in the case of a stationary solution of the spin motion (*i.e.*,
 2806 the spin precession axis) s satisfies [19] (Fig. 8.20)
 2807

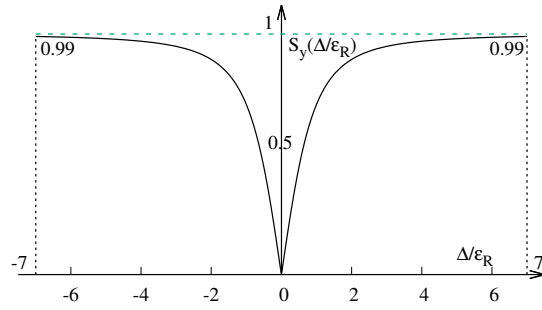
Fig. 8.20 Modulus of the horizontal spin component. $s = 1/2$ at distance $\Delta = \pm\sqrt{3}\epsilon_R$ from $G\gamma_R$



$$s^2 = \frac{1}{1 + \frac{\Delta^2}{|\epsilon_R|^2}} \quad (8.48)$$

wherein $\Delta = G\gamma - G\gamma_R$ is the distance to the resonance. The resonance width is a

Fig. 8.21 Dependence of polarization on the distance to the resonance. For instance $S_y = 0.99$, 1% depolarization, corresponds to $\Delta = 7|\epsilon_R|$. On the resonance, $\Delta = 0$, the precession axis lies in the median plane, $S_y = 0$



2808

2809

2810

measure of its strength (Fig. 8.21). The quantity of interest is the angle, ϕ , of the spin precession direction to the vertical axis, given by (Fig. 8.21)

$$\cos \phi(\Delta) \equiv S_y(\Delta) = \sqrt{1 - s^2} = \frac{\Delta/|\epsilon_R|}{\sqrt{1 + \Delta^2/|\epsilon_R|^2}} \quad (8.49)$$

2811

2812

2813

2814

On the resonance, $\Delta = 0$, the spin precession axis lies in the bend plane: $\phi = \pm\pi/2$. $S_y = 0.99$ (1% depolarization) corresponds to a distance to the resonance $\Delta = 7|\epsilon_R|$, and spin precession axis at an angle $\phi = \arccos(0.99) = 8^\circ$ from the vertical.

Conversely,

$$\frac{\Delta^2}{|\epsilon_R|^2} = \frac{S_y^2}{1 - S_y^2} \quad (8.50)$$

The precession axis is common to all spins, S_y is a measure of the polarization along the vertical axis,

$$S_y = \frac{N^+ - N^-}{N^+ + N^-}$$

2815 wherein N^+ and N^- denote the number of particles in spin states $\frac{1}{2}$ and $-\frac{1}{2}$ respec-
2816 tively.

2817 *Spin motion through weak resonances*

Depolarizing resonances are weak up to several GeV in a weak focusing synchrotron, as the radial and/or longitudinal fields, which stem from a small radial field index and from dipole fringe fields, are weak. Spin motion $S_y(\theta)$ through a resonance in that case (*i.e.*, assuming $S_{y,f} \approx S_{y,i}$, with $S_{y,f}$ and $S_{y,i}$ the asymptotic vertical spin component values respectively upstream and downstream of the resonance) can be calculated in terms of the Fresnel integrals

$$C(x) = \int_0^x \cos\left(\frac{\pi}{2}t^2\right) dt, \quad S(x) = \int_0^x \sin\left(\frac{\pi}{2}t^2\right) dt$$

namely, with the origin of the orbital angle taken at the resonance [19] (Fig. 8.22)

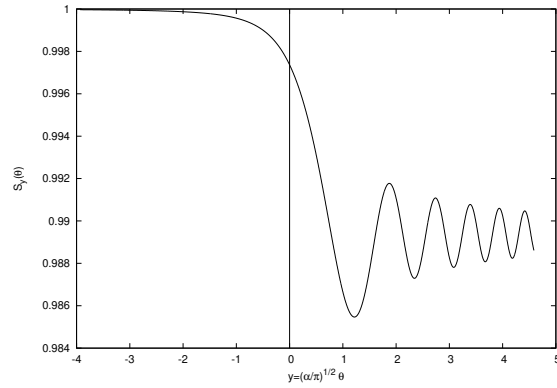


Fig. 8.22 Vertical component of spin motion $S_y(\theta)$ through a weak depolarizing resonance (after Eq. 8.51). The vertical bar is at the location of the resonance, which coincides with the origin of the orbital angle

2818

$$\begin{aligned} \text{if } \theta < 0 : \left(\frac{S_y(\theta)}{S_{y,i}} \right)^2 &= 1 - \frac{\pi}{\alpha} |\epsilon_R|^2 \left\{ \left[0.5 - C\left(-\theta \sqrt{\frac{\alpha}{\pi}}\right) \right]^2 + \left[0.5 - S\left(-\theta \sqrt{\frac{\alpha}{\pi}}\right) \right]^2 \right\} \\ \text{if } \theta > 0 : \left(\frac{S_y(\theta)}{S_{y,i}} \right)^2 &= 1 - \frac{\pi}{\alpha} |\epsilon_R|^2 \left\{ \left[0.5 + C\left(\theta \sqrt{\frac{\alpha}{\pi}}\right) \right]^2 + \left[0.5 + S\left(\theta \sqrt{\frac{\alpha}{\pi}}\right) \right]^2 \right\} \end{aligned} \quad (8.51)$$

2819 In the asymptotic limit,

$$\frac{S_y(\theta)}{S_{y,i}} \xrightarrow{\theta \rightarrow \infty} 1 - \frac{\pi}{\alpha} |\epsilon_R|^2 \quad (8.52)$$

2820 which identifies with the development of Froissart-Stora formula $P_f/P_i = 2 \exp(-\frac{\pi}{2} \frac{|\epsilon_R|^2}{\alpha}) -$
2821 1, to first order in $|\epsilon_R|^2/\alpha$. This approximation holds in the limit that higher order
2822 terms can be neglected, *viz.* $|\epsilon_R|^2/\alpha \ll 1$.

2823 **8.2 Exercises**2824 **Preliminaries**

- 2825 • Zgoubi users' guide at hand, when setting up the input data files to work out
 2826 the exercises, is a must-have. PART B of the guide in particular, details the
 2827 formatting of the input data lists following keywords (a few keywords only, for
 2828 instance FAISCEAU, MARKER, YMY, do not require additional data), and gives
 2829 the units to be used.
- 2830 • About keywords: by "keyword" it is meant, the name of the optical elements,
 2831 or I/O procedures, or commands, as they appear in simulation input data file.
 2832 Keywords are most of the time referred to without any additional explanation: it
 2833 is understood that the users' guide is at hand, and details regarding the use and
 2834 functioning to be sought there: in PART A of the guide, as to what a particular
 2835 keyword does and how it does it; in PART B as to the formatting of the data
 2836 list under a particular keyword. The users' guide INDEX is a convenient tool to
 2837 navigate through the keywords.
- 2838 – The notation KEYWORDS[ARGUMENT1, ARGUMENT2, ...]: it uses the
 2839 nomenclature found in the Users' Guide, Part B. Consider a couple of exam-
 2840 ples:
 2841 · OBJET[KOBJ=1] stands for keyword OBJET, and the value of KOBJ=1
 2842 retained here;
 2843 · OPTIONS[CONSTY=ON] stands for keyword OPTIONS, and the option
 2844 retained here, CONSTY, switched ON.
- 2845 – The keyword INCLUDE is used in many simulation input data files. The reason
 2846 is mostly to reduce the length of these files. It may always be replaced by the
 2847 sequence that it INCLUDEs.
- Coordinate Systems: two sets of coordinate notations are used in the exercises,

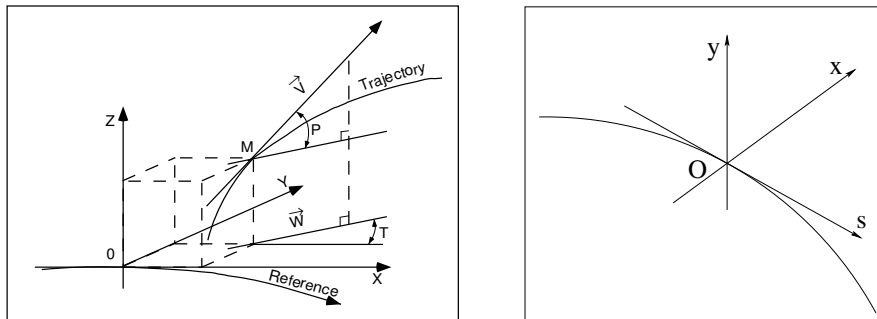


Fig. 8.23 Zgoubi Cartesian frame (O;X,Y,Z), and moving frame (O;s,x,y)

- 2849 – on the one hand (and, in the Solutions Section mostly), zgoubi's (Y,T,Z,P,X,D)
 2850 coordinates in the optical element reference frame (O;X,Y,Z), the very frame
 2851 in which the optical element field $\mathbf{E}(X, Y, Z)$ and/or $\mathbf{B}(X, Y, Z)$ is defined (the
 2852 origin for X depends on the optical element). Particle coordinates in this frame
 2853 can be
- 2854 · either Cartesian, in which case X, Y (angle T) and Z (angle P) denote
 - 2855 respectively the longitudinal, transverse horizontal and vertical coordinates,
 - 2856 · or cylindrical, in which case, given m the projection of particle position M
 - 2857 in the $Z=0$ plane, Y denotes the radius: $Y = |\mathbf{Om}|$, whereas X denotes the
 - 2858 **OX-Om** angle (and, yes, the nature of the variables named X and Y in the
 - 2859 source code does change);

Note: the sixth zgoubi's coordinate above is

$$D = \frac{\text{particle rigidity}}{BORO}$$

2860 with BORO a reference rigidity, the very first numerical datum to appear in
 2861 any zgoubi sequence, as part of the definition of initial particle coordinates by
 2862 OBJET or MCOBJET. BORO may sometimes be denoted $B\rho_{\text{ref}}$, depending
 2863 upon the context. Note that D-1 identifies with the above $\delta p/p$.

- 2864 – on the other hand (and, in the exercise assignments mostly), the conventional
 2865 $(x, x', y, y', \delta l, \delta p/p)$ coordinates in the moving frame (O;s,x,y) or close variants.

2866 Comments are introduced wherever deemed necessary (hopefully, often enough)
 2867 in an effort to lift potential ambiguities regarding coordinate notations.

2868 8.1 Optical Functions in a Weak Focusing Synchrotron

- 2869 (a) Demonstrate the approximation for the transport matrix, Eq. 8.31.
 2870 (b) Demonstrate Eq. 8.35.

2871 8.2 Construct Saturne I synchrotron. Spin Resonances

2872 (a) Construct a model of the Saturne I synchrotron, using DIPOLE. Use Fig. 8.24
 2873 as a guidance, and parameters given in Tab. 8.2. Assume that the reference orbit is
 2874 the same at all energies, on nominal radius, 841.93 cm. It is judicious (although in
 2875 no way an obligation) to take RM=841.93 in DIPOLE.

2876 Check the correctness of the model by producing the lattice parameters of the
 2877 ring. TWISS can be used for that. Compare with the lattice parameters given in
 2878 Tab. 8.2.

2879 Produce a tune scan of the wave numbers over the radial field index $0.5 \leq n \leq$
 2880 0.757 operation range. The REBELOTE do loop can be used for that, to repeatedly
 2881 change n and compute a MATRIX. Compare with theoretical expectations.

- 2882 (b) Produce a graph of the betatron functions along the Saturne I cell. Provide
 2883 checks of the correctness of the computation.

2884 Check the theoretical periodic dispersion (Eq. 8.14) against the radial distance
 2885 between on- and off-momentum closed orbits obtained from tracking. Provide a plot
 2886 of the dispersion function.

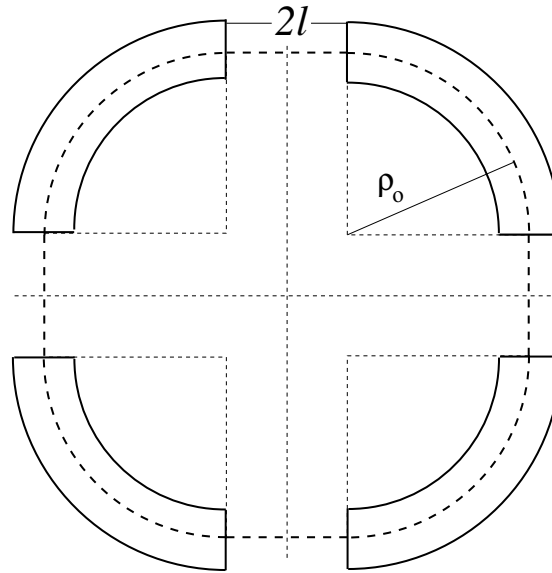


Fig. 8.24 A schematic layout of Saturne I, a $2\pi/4$ axial symmetry structure, comprised of 4 radial field index 90 deg dipoles and 4 drift spaces. The cell in the simulation exercises is taken as a $\pi/4$ quadrant: l -drift/ 90° -dipole/ l -drift

Table 8.2 Parameters of Saturne 1 weak focusing synchrotron [9]. ρ_0 denotes the reference bending radius in the dipole; the reference orbit, field index, wave numbers, etc., are taken along that radius

Orbit length, C	cm	6890
Equivalent radius, R	cm	1096.58
Straight section length, $2l$	cm	400
Magnetic radius, ρ_0	cm	841.93
R/ρ_0		1.30246
Field index n , nominal value		0.6
Wave numbers, $\nu_x; \nu_y$		0.724; 0.889
Stability limit		$0.5 < n < 0.757$
Injection energy	MeV	3.6
Field at injection	kG	0.0326
Top energy	GeV	2.94
Field at top energy	kG	14.9
Field ramp at injection	kG/s	20
Synchronous energy gain	keV/turn	1.160
RF harmonic		2

2887 (c) Additional verifications regarding the model.
 2888 Produce a graph of the field $B(s)$

2889 - along the on-momentum closed orbit, and along off-momentum chromatic closed
2890 orbits, across a cell;

2891 - along orbits at large horizontal excursion;

2892 - along orbits at large vertical excursion.

2893 For all these cases, verify qualitatively, from the graphs, that $B(s)$ appears as
2894 expected.

(d) Justify considering the betatron oscillation as sinusoidal, namely,

$$y(\theta) = A \cos(\nu_y \theta + \phi)$$

2895 wherein $\theta = s/R$, $R = \oint ds/2\pi$.

2896 Find the value of the horizontal and vertical betatron functions, resulting from
2897 that approximation. Compare with the betatron functions obtained in (b).

2898 (e) Produce an acceleration cycle from 3.6 MeV to 3 GeV, for a few particles
2899 launched on the a common $10^{-4} \pi\text{m}$ vertical initial invariant, with small horizontal
2900 invariant. Ignore synchrotron motion (CAVITE[IOPT=3] can be used in that case).
2901 Take a peak voltage $\hat{V} = 200 \text{ kV}$ (unrealistic though, as it would result in a nonphysical
2902 \hat{B} (Eq. 8.37)) and synchronous phase $\phi_s = 150 \text{ deg}$ (justify $\phi_s > \pi/2$). Add spin,
2903 using SPNTRK, in view of the next question, (f).

2904 Check the accuracy of the betatron damping over the acceleration range, compared
2905 to theory.

2906 How close to symplectic the numerical integration is (it is by definition *not*
2907 symplectic, being a truncated Taylor series method [20, Eq. 1.2.4]), depends on the
2908 integration step size, and on the size of the flying mesh in the DIPOLE method [20,
2909 Fig. 20]; check a possible departure of the betatron damping from theory as a function
2910 of these parameters.

2911 Produce a graph of the the evolution of the horizontal and vertical wave numbers
2912 during the acceleration cycle.

2913 (f) Using the raytracing material developed in (e), but for a peak voltage $\hat{V} =$
2914 20 kV , produce a graph of the value of the vertical spin component of the particles
2915 as a function of $G\gamma$, over the acceleration range from 3.6 MeV to 3 GeV.

2916 Produce a graph of the average value of S_Z over that 200 particle set, as a function
2917 of $G\gamma$. Indicate on that graph the location of the resonant $G\gamma_R$ values.

2918 (g) Based on the simulation file used in (f), simulate the acceleration of a single
2919 particle, through the intrinsic resonance $G\gamma_R = 4 - \nu_Z$, from a few thousand turns
2920 upstream to a few thousand turns downstream.

2921 Perform this resonance crossing for five different values of the particle invariant,
2922 namely: $\epsilon_Z/\pi = 2, 10, 20, 40, 200 \mu\text{m}$.

2923 Compute P_f/P_i in each case, check the dependence on ϵ_Z against theory. Compute
2924 the resonance strength in each case, check the dependence on ϵ_Z against theory.

2925 Re-do this crossing simulation for a different crossing speed (take for instance
 2926 $\hat{V} = 10$ kV) and a couple of vertical invariant values, compute P_f/P_i so obtained.
 2927 Check the crossing speed dependence of P_f/P_i against theory.

2928 (h) Plot the turn-by-turn vertical spin component motion $S_Z(\text{turn})$ across the
 2929 resonance $G\gamma_R = 4 - \nu_Z$, in a weakly depolarizing case, $P_f \approx P_i$. Show that it
 2930 satisfies Eq. 8.51. Match the data to the latter to get the vertical betatron tune ν_y , and
 2931 the location of the resonance $G\gamma_R$.

2932 (i) Track a few particles at fixed energy, at distances from the resonance $G\gamma_R =$
 2933 $4 - \nu_y$ of up to a $7 \times \epsilon_R$ (this distance corresponds to 1% depolarization).

2934 Produce on a common graph the spin motion $S_Z(\text{turn})$ for all these particles, as
 2935 observed at some azimuth along the ring.

2936 Produce a graph of $\langle S_y \rangle|_{\text{turn}}(\Delta)$ (as in Fig. 8.21).

Produce the vertical betatron tune ν_y , and the location of the resonance $G\gamma_R$,
 obtained from a match of these tracking trials to the theoretical (Eq. 8.49)

$$\langle S_y \rangle (\Delta) = \frac{\Delta}{\sqrt{|\epsilon_R|^2 + \Delta^2}}$$

2937 8.3 Construct the ZGS synchrotron. Spin Resonances

2938 (a) Construct an approximate model of the ZGS synchrotron, using DIPOLE.
 2939 Use Figs. 8.25, 8.26 as a guidance, and parameters given in Tab. 8.3. Assume that
 2940 the reference orbit is the same at all energies, on nominal radius, 2076 cm. It is
 2941 judicious (although in no way an obligation) to take RM=2076 in DIPOLE. (Note
 2942 that in reality, unlike the present assumption for this exercise, the reference orbit in
 2943 ZGS would be moved outward during acceleration [21].)

2944 Check the correctness of the model by producing the lattice parameters of the
 2945 ring. TWISS can be used for that. Compare with the lattice parameters given in
 2946 Tab. 8.3.

2947 (b) Produce a graph of the betatron functions along the ZGS cell. Provide checks
 2948 of the correctness of the computation.

2949 Check the theoretical periodic dispersion (Eq. 8.14) against the radial distance
 2950 between on- and off-momentum closed orbits obtained from tracking. Provide a plot
 2951 of the dispersion function.

2952 (c) Additional verifications regarding the model.

2953 Produce a graph of the field $B(s)$

2954 - along the on-momentum closed orbit, and along off-momentum chromatic closed
 2955 orbits, across a cell;

2956 - along orbits at large horizontal excursion;

2957 - along orbits at large vertical excursion.

2958 For all these cases, verify qualitatively, from the graphs, that $B(s)$ appears as
 2959 expected.

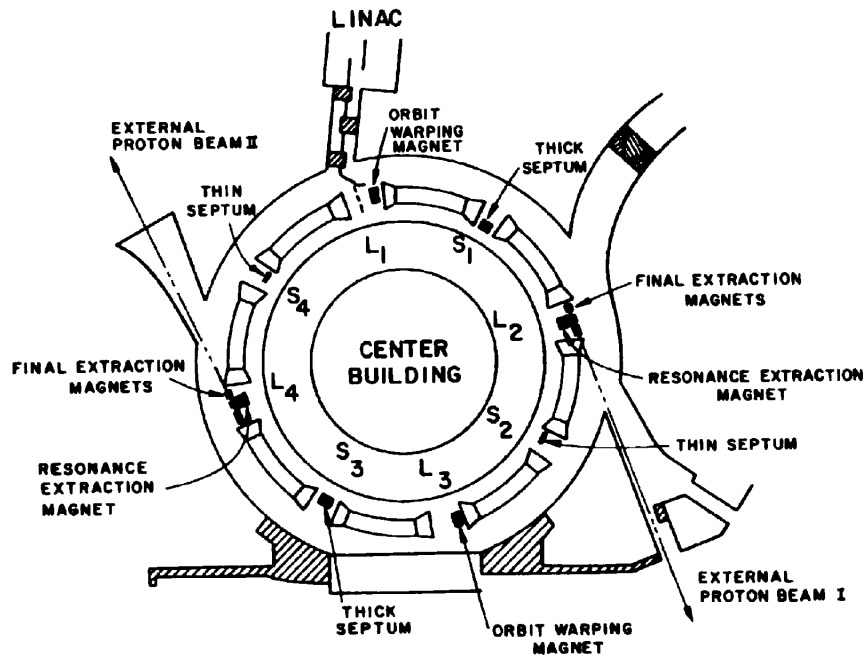


Fig. 8.25 A schematic layout of the ZGS [18], a $\pi/2$ -periodic structure, comprised of 8 zero-index dipoles, 4 long and 4 short straight sections

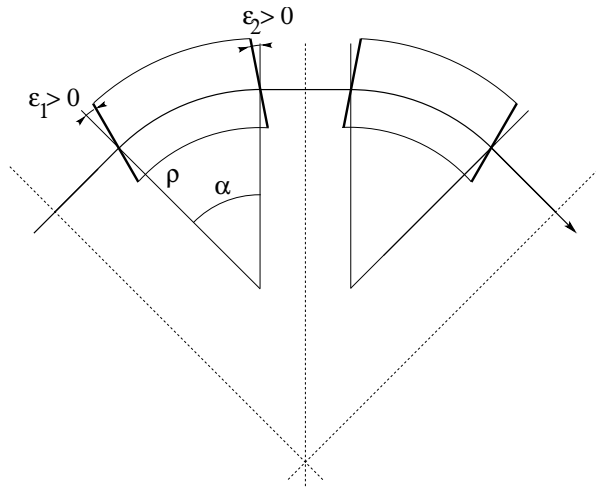


Fig. 8.26 A sketch of Saturne I cell layout. In defining the entrance and exit faces (EFBs) of the magnet, beam goes from left to right. Wedge angles at the long straight sections (ϵ_1) and at the short straight sections (ϵ_2) are different

Table 8.3 Parameters of the ZGS weak focusing synchrotron after Refs. [21, 22] [18, pp. 288-294, p. 716] (2nd column, when they are known) and in the present simplified model and numerical simulations (3rd column). Note that the actual orbit is skewed (moves) during ZGS acceleration cycle, tunes change as well - this is not the case in the present modeling

		From Refs. [21, 22]	Simplified model
Injection energy	MeV		50
Top energy	GeV		12.5
$G\gamma$ span		1.888387 - 25.67781	
Length of central orbit	m	171.8	170.90457
Length of straight sections, total	m	41.45	40.44
<i>Lattice</i>			
Wave numbers $\nu_x; \nu_y$		0.82; 0.79	0.849; 0.771
Max. $\beta_x; \beta_y$	m		32.5; 37.1
<i>Magnet</i>			
Length	m	16.3	16.30486 (magnetic)
Magnetic radius	m	21.716	20.76
Field min.; max.	kG	0.482; 21.5	0.4986; 21.54
Field index			0
Yoke angular extent	deg	43.02590	45
Wedge angle	deg	≈ 10	13 and 8
<i>RF</i>			
Rev. frequency	MHz	0.55 - 1.75	0.551 - 1.751
RF harmonic $h = \omega_{rf} / \omega_{rev}$			8
Peak voltage	kV	20	200
B-dot, nominal/max.	T/s	2.15/2.6	
Energy gain, nominal/max.	keV/turn	8.3/10	100
Synchronous phase, nominal	deg		150
<i>Beam</i>			
$\epsilon_x; \epsilon_y$ (at injection)	$\pi\mu_z$ m		25; 150
Momentum spread, rms			3×10^{-4}
Polarization at injection	%	>75	100
Radial width of beam (90%), at inj.	inch	2.5	$\sqrt{\beta_x \epsilon_x / \pi} = 1.1$

(d) Justify considering the betatron oscillation as sinusoidal, namely,

$$y(\theta) = A \cos(\nu_y \theta + \phi)$$

2960 wherein $\theta = s/R$, $R = \oint ds/2\pi$.

2961 Find the value of the horizontal and vertical betatron functions, resulting from
2962 that approximation. Compare with the betatron functions obtained in (b).

2963 (e) Produce an acceleration cycle from 50 MeV to 17 GeV about, for a few particles
2964 launched on the a common $10^{-5} \pi$ m vertical initial invariant, with small horizontal
2965 invariant. Ignore synchrotron motion (CAVITE[IOPT=3] can be used in that case).
2966 Take a peak voltage $\hat{V} = 200$ kV (this is unrealistic but yields 10 times faster
2967 computing than the actual $\hat{V} = 20$ kV, Tab. 8.3) and synchronous phase $\phi_s = 150$ deg
2968 (justify $\phi_s > \pi/2$). Add spin, using SPNTRK, in view of the next question, (f).

2969 Check the accuracy of the betatron damping over the acceleration range, compared
2970 to theory. How close to symplectic the numerical integration is (it is by definition
2971 *not* symplectic), depends on the integration step size, and on the size of the flying
2972 mesh in the DIPOLE method [20, Fig. 20]; check a possible departure of the betatron
2973 damping from theory as a function of these parameters.

2974 Produce a graph of the the evolution of the horizontal and vertical wave numbers
2975 during the acceleration cycle.

2976 (f) Using the raytracing material developed in (e): produce a graph of the vertical
2977 spin component of the particles, and the average value over that 200 particle set, as
2978 a function of $G\gamma$. Indicate on that graph the location of the resonant $G\gamma_R$ values.

2979 (g) Based on the simulation file used in (f), simulate the acceleration of a single
 2980 particle, through one particular intrinsic resonance, from a few thousand turns
 2981 upstream to a few thousand turns downstream.

2982 Perform this resonance crossing for different values of the particle invariant.
 2983 Determine the dependence of final/initial vertical spin component value, on the
 2984 invariant value; check against theory.

2985 Re-do this crossing simulation for a different crossing speed. Check the crossing
 2986 speed dependence of final/initial vertical spin component so obtained, against theory.

2987 (h) Introduce a vertical orbit defect in the ZGS ring.

2988 Find the closed orbit.

2989 Accelerate a particle launched on that closed orbit, from 50 MeV to 17 GeV about,
 2990 produce a graph of the vertical spin component.

2991 Select one particular resonance, reproduce the two methods of (g) to check the
 2992 location of the resonance at $G\gamma_R = \text{integer}$, and to find its strength.

2993 References

- 2994 1. Veksler, V.: A new method of acceleration of relativistic particles. J. of Phys. USSR 9 153-158
 2995 (1945)
- 2996 2. McMillan, E. M.: The Synchrotron. Phys. Rev. 68 143-144 (1945)
- 2997 3. Kerst, D. W.: The Acceleration of Electrons by Magnetic Induction.. Phys. Rev., 60, 47-53
 2998 (1941)
- 2999 4. Richardson, J.R., et al.: Frequency Modulated Cyclotron. Phys. Rev. 69: 669 (1946)
- 3000 5. Sessler, A., Wilson, E.: Engines of Discovery. A Century of Particle Accelerators. World
 3001 Scientific, 2007
- 3002 6. ***** completer ***** Archives historiques CEA. Copyright CEA/Service de documen-
 3003 tation - FAR_SA_N_00248
- 3004 7. Froissart, M. and Stora, R.: Dépolarisation d'un faisceau de protons polarisés dans un syn-
 3005 chrotron. Nucl. Inst. Meth. 7 (1960) 297.
- 3006 8. Ratner, L.G. and Khoe, T.K.: Acceleration of Polarized Protons in the Zero Gradient Syn-
 3007 chrotron. Procs. PAC 1973 Conference, Washington (1973).
 3008 http://accelconf.web.cern.ch/p73/PDF/PAC1973_0217.PDF
- 3009 9. Bruck H., Debraine P., Levy-Mandel R., Lutz J., Podliasky I., Prevot F., Taieb J., Winter S.D.,
 3010 Maillet R., Caractéristiques principales du Synchrotron Ã Protons de Saclay et résultats
 3011 obtenus lors de la mise en route, rapport CEA no.93, CEN-Saclay, 1958.
- 3012 10. Khoe, T.K., et al.: Acceleration of polarized protons to 8.5 GeV/c, Particle Accelerators, 1975,
 3013 Vol. 6, pp. 213-236.
- 3014 11. Suddeth, D.E., et als.: Pole face winding equipment for eddy current correction at the Zero
 3015 Gradient Synchrotron. Procs. PAC 1973 Conference, Washington (1973).
 3016 http://accelconf.web.cern.ch/p73/PDF/PAC1973_0397.PDF
- 3017 12. Rauchas, A.V. and Wright, A.J.: Betatron tune profile control in the Zero Gradient Synchrotron
 3018 (ZGS) using the main magnet pole face windings. Procs. PAC1977 conference, IEEE Trans.
 3019 on Nucl. Science, VoL.NS-24, No.3, June 1977
- 3020 13. Floquet, G.: Sur les équations différentielles linéaires à coefficients périodiques. Annales
 3021 scientifiques de l'E.N.S. 2e série, tome 12 (1883), p. 47-88.
 3022 http://www.numdam.org/item?id=ASENS_1883_2_12_47_0
- 3023 14. Cohen, D. : Feasibility of Accelerating Polarized Protons with the Argonne ZGS. Review of
 3024 Scientific Instruments 33, 161 (1962).// <https://doi.org/10.1063/1.1746524>